Evaporation-driven solutocapillary flow of thin liquid films over curved substrates

Mariana Rodríguez-Hakim,[1,*] Joseph M. Barakat,[1,*,†] Xingyi Shi,[1]
Eric S. G. Shaqfeh,[1,2,3,‡] and Gerald G. Fuller[1,§]
[1]*Department of Chemical Engineering, Stanford University, Stanford, California 94305, USA*
[2]*Department of Mechanical Engineering, Stanford University, Stanford, California 94305, USA*
[3]*Institute for Computational and Mathematical Engineering, Stanford University, Stanford, California 94305, USA*

(Received 21 June 2018; published 13 March 2019)

Evaporative loss of a volatile solvent can induce concentration inhomogeneities that give rise to spatial gradients in surface tension and subsequent solutocapillary Marangoni flows. This phenomenon is studied in the context of ultrathin liquid films resting atop curved convex substrates in contact with a fluid reservoir. Experiments are conducted with low-molecular-weight polydimethylsiloxane (silicone oil) mixtures composed of a volatile solvent and trace amounts of a nonvolatile solute. A theoretical model based on the thin-film approximation is developed, incorporating the effects of evaporative mass loss, gravity, capillarity, van der Waals forces, species diffusion, and Marangoni stresses. The spatiotemporal evolution of this system is studied by modulating the rate of evaporation of the volatile species and the bulk solute volume fraction in the mixture. The experiments and accompanying numerical simulations reveal that both Marangoni stresses and stabilizing van der Waals interactions between the substrate and the free surface can induce flow reversal and film regeneration. Their relative contribution is modulated by the solutocapillary Marangoni number, which is proportional to the bulk concentration of nonvolatile species in the mixture. Furthermore, it is revealed that increasing the rate of evaporation enhances the volumetric flow rate from thicker, solvent-rich areas towards thinner, solute-rich regions of the film. Although quantitative differences between the theory and the experiments are observed within certain ranges of the controlled parameters, the model qualitatively reproduces the flow regimes observed in the experiments and elucidates the complex interplay among the various physical forces.

DOI: 10.1103/PhysRevFluids.4.034002

I. INTRODUCTION

Solutocapillary Marangoni flows arise when a nonuniform distribution of chemical species in solution creates gradients in surface tension. Perhaps the most well-known example is the tears of wine phenomenon, in which surface-tension gradients are induced by a concentration imbalance of water and ethanol [1,2]. Solutal Marangoni flows are also prevalent in spin-cast polymer films [3], thin coatings [4], and paints [5–7]. Understanding how these flows couple to other physical processes, such as evaporation and pressure-driven flow, has both fundamental and practical value

[*]These authors contributed equally to this work.
[†]Present address: University of California, Santa Barbara, California 93106, USA.
[‡]esgs@stanford.edu
[§]ggf@stanford.edu

[8,9]. In the coating application, for example, it is often desirable to apply smooth homogeneous liquid films that dry uniformly. However, there are instances in which defects such as craters and ridges form as a result of nonuniform drying [4–7]. Spatial inhomogeneities in species concentration are established due to the different rates of evaporation of each component in the mixture. Since surface tension depends on the local species concentration at the interface, concentration gradients in turn induce surface-tension gradients and subsequent Marangoni flows.

Early theoretical and experimental studies were conducted in an effort to understand the dominant mechanisms that give rise to surface-tension gradients in drying paint layers. An experimental study of the leveling kinetics of decorative paints was conducted by Overdiep [5], who identified solvent evaporation as the driving force for the development of inhomogeneities in the applied layer thickness. These effects were also studied theoretically by Howison *et al.* [6], Evans *et al.* [7], and Eres *et al.* [4], who derived mathematical models based on classical lubrication theory for paints consisting of a volatile solvent and a nonvolatile resin. Since the resin has, in these cases, a higher surface tension than the solvent, Marangoni stresses drive flow from thicker, solvent-rich regions of the film to thinner, resin-rich areas. In addition to evaporation and solutocapillarity, the effects of viscosification, solvent diffusivity, gravity, and capillarity were incorporated. Simulations for periodic geometries were conducted using initial layer thicknesses on the order of tens of microns and initial resin concentrations of around 50 vol %.

Evaporation-induced Marangoni stresses can give rise to flow reversal and instability in thin liquid films. Hu and Larson discovered a reversal of the coffee-ring effect, whereby a recirculatory (thermocapillary) Marangoni flow drives solute particles towards the centerline of an evaporating sessile droplet [10–12]. The same effect can be achieved in multicomponent droplets through the analogous solutocapillary mechanism [13,14]. de Gennes was the first to predict (using scaling arguments) a solutocapillary instability in polymeric films with a volatile solvent [3]. Significantly, he claimed that the proposed instability should dominate over thermally driven (Bénard-Marangoni) instabilities below the glass-transition temperature, provided that the polymer does not adsorb to the solution free surface. Serpetsi and Yiantsios later expounded upon de Gennes's work by performing direct numerical calculations (as well as a linear stability analysis) of a two-component liquid with a slowly evaporating solvent [15]. Their study revealed that, at dilute solute concentrations, spatial and temporal oscillations in the film thickness can arise due to the synergistic interplay between capillary-pressure and surface-tension gradients. The minimum surface-tension gradient required for the onset of flow reversal, that is, flow *against* the pressure gradient, is a function of the rate of evaporation. It was found that increasing the rate of evaporation has a complex effect on the reversal behavior, as it accelerates the formation of surface-tension gradients and the rate of viscosification, which respectively enhances and dampens film-thickness oscillations [4–7,15].

The effect of substrate slope and curvature can have surprising consequences in solutocapillary flows, particularly in cases where a thin film deposited on the substrate is in contact with a bulk reservoir of liquid. Essentially, the inclined or curved geometry creates differentials in film thickness and film curvature between a thin meniscus region and a thicker bulk region, which in turn introduce additional pressure gradients that are not observed in horizontal films [16]. Parks and Wayner [17] developed a model to study surface-tension-driven flow of an evaporating film composed of 98% decane and 2% tetradecane over a heated inclined silicon wafer. They showed that even small quantities of a nonvolatile impurity (tetradecane) could enhance surface stress, producing markedly different film profiles than those which would occur in pure decane. Quantitative studies of the classical tears of wine phenomenon were later carried out by Fournier and Cazabat [2] and Vuilleumier *et al.* [18]. In these works, curved or tilted planar glass substrates were partially submerged in mixtures of water and ethanol at varying volume fractions. As surface-tension gradients developed due to the changing alcohol concentration, a thin liquid film (20–100 μm in thickness) was observed to climb vertically upward along the meniscus region, away from the fluid reservoir. Fanton and Cazabat later derived a simple expression for the velocity of a fluid front climbing up a vertically inclined plane, solely under the action of evaporation-induced solutocapillary stresses [19]. Although their model did not account for additional pressure gradients arising from

gravitational or capillary effects, their results quantitatively agreed with experimental observations for alkane mixtures and water-ethanol systems. The stability characteristics of evaporating thin films spreading over inclined plates in contact with a bulk fluid reservoir were studied in detail by Hosoi and Bush [20], revealing a rich spectrum of flow behavior (longitudinal rolls, laterally drifting ridge structures, falling tears, and vertically propagating transverse waves).

The aforementioned studies have unequivocally demonstrated the presence and basic mechanism of evaporation-driven solutocapillary flows in relatively simple geometries. However, several important questions remain. For one, it remains unclear at what point Marangoni stresses begin to dominate over other physical forces (e.g., pressure forces) in the presence of evaporation. This issue is particularly relevant in very thin films at low concentrations of a nonvolatile impurity, wherein Marangoni stresses are expected to be relatively weak. Virtually all of the studies mentioned above have focused on films thicker than a micron, with solute concentrations above 2 vol %. However, many spin-coating processes and microfabrication technologies rely on the application of highly uniform submicron films (in some cases, at very dilute concentrations of a solute species). Moreover, liquid films of submicron thickness are commonly found in biological systems [21–23]. One example is the human tear film, which has a thickness between 0.5 and 5.0 μm and an average dissolved protein concentration of roughly 9 mg/mL (approximately 0.1 wt.%) [21,24].

Second, the influence of nonhydrodynamic (e.g., van der Waals) forces on the film dynamics remains only partially understood. Such forces are expected to become significant in ultrathin films with dimensions on the order of 100 nm [16]. van der Waals forces mediated through the liquid can give rise to disjoining (or conjoining) pressures between the substrate and free surface, which can stabilize (or destabilize) the film depending on the chemical nature of the substrate-liquid pair [25,26]. Although there has been a plethora of studies on the role of van der Waals forces in dewetting phenomena [27–34], the influence of a disjoining pressure between the substrate and free surface has not yet been examined in the context of solutocapillary phenomena.

Finally, the role of the contact line on the dynamics of evaporating thin films remains a significant (and, in some cases, obfuscating) issue. It is well known that the specific nature of the contact line can have dramatic consequences on thin-film flows [9,35]. Many interesting observations of solutocapillary phenomena are intrinsically associated with the so-called contact-line pinning, an important example being the aforementioned coffee-ring reversal phenomenon [12,13]. Oftentimes, the contact line (and contact angle) is highly sensitive to the experimental conditions, including substrate roughness, cleanliness, and wettability [36], and may obscure interpretation of thin-film measurements. It is therefore desirable to eliminate the effect of the contact line in circumstances where other physical driving forces (evaporation, surface-tension gradients, and pressure gradients) are of interest.

In this article we utilize both experiments and theory to understand the synergistic action of evaporation, pressure, and surface tension in creating and sustaining solutocapillary flows in thin films of a binary liquid mixture containing trace amounts of a nonvolatile species. A previously reported apparatus, the dynamic fluid-film interferometer [37], is utilized in the present study to examine the evolution of thin films on spherical convex substrates in contact with a fluid reservoir. The geometry used in this study includes no pinned contact lines and allows for axisymmetric liquid motions. In our experiments, a bulk liquid mixture continuously supplies fluid to a thin film through a delicate interplay of evaporation, pressure-driven flow (due to both capillary action and van der Waals forces), and solutocapillary Marangoni flow. The use of a convex surface allows liquid to accumulate at the substrate apex, providing a useful platform for tracking fluid fluxes. We analyze the importance of these various physical effects by complementing our experiments with a numerical model rooted in thin-film theory. In particular, we restrict our attention to stable axisymmetric flows, leaving consideration of unstable asymmetric flows to a possible future study.

The remainder of the article is organized as follows. In Sec. II we describe the experimental setup and introduce the relevant geometric and material properties that govern the flow physics. Experiments are conducted using binary silicone-oil mixtures deposited onto optical lenses of constant radius of curvature. In Sec. III a theoretical model for the spatiotemporal evolution of

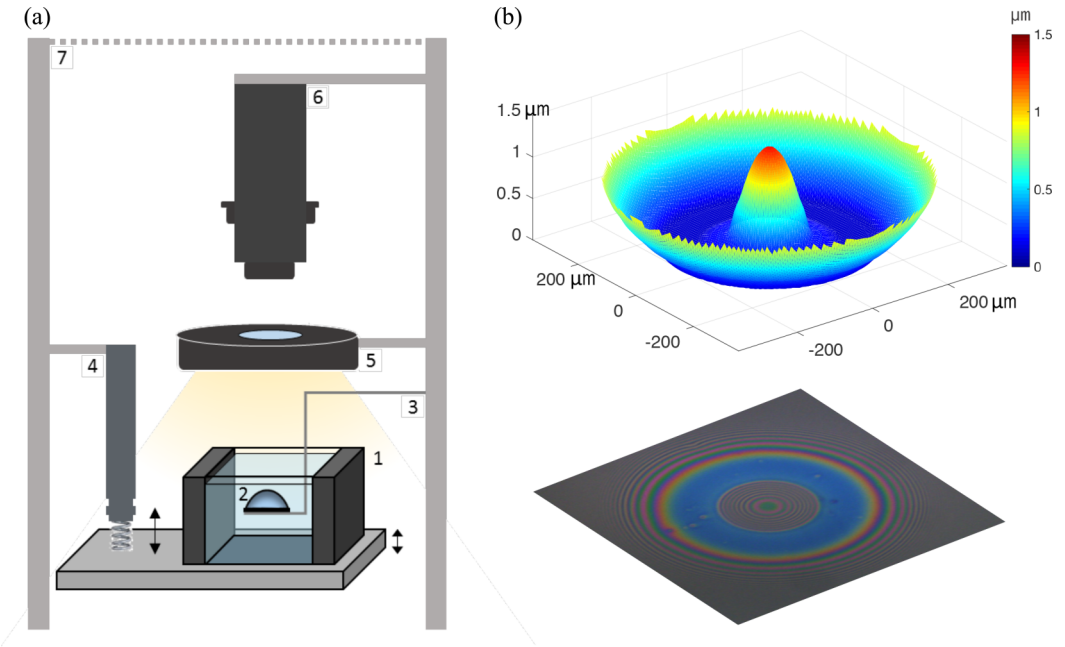

FIG. 1. (a) The dynamic fluid-film interferometer, a custom-built apparatus [37], is used to create thin liquid films between a spherical solid substrate and an initially planar free surface. Labeled components in the figure correspond to 1, Delrin chamber; 2, fused-silica substrate; 3, substrate holder; 4, motorized actuator; 5, light source; 6, top camera; and 7, DFI cover. (b) On the bottom, white-light interferometry is used to map color images recorded from the top camera to film thickness profiles. On the top, an image-processing script is used to visualize the spatiotemporal evolution of the entrained liquid film.

the film thickness and solute concentration is developed under the auspices of thin-film theory. The model takes into account the effects of gravity, capillarity, van der Waals forces, species diffusion, and Marangoni stresses. The effects of densification and viscosification, arising from differences in material properties between the two liquid species, are not incorporated into the model. The resulting system of evolution equations is solved numerically using the finite-difference method. In Sec. IV we compare our experimental measurements to the theoretical predictions. A discussion of our results is given in Sec. V. We find that the model qualitatively reproduces the flow regimes observed in the experiments and reveals the dominant driving forces. A tug-of-war between pressure-driven flow and Marangoni flow is modulated by the solutocapillary Marangoni number, which is proportional to the concentration of nonvolatile species in the mixture. The rate of evaporation qualitatively affects these dynamics and controls the rate at which solutocapillary stresses are generated. Quantitative differences between the theory and the experiments are observed; we attribute these differences to the simplifying assumptions made in the model, as well as uncertainties in the values of some of the dimensionless parameters. Suggestions for improvements of the model, directions for future study, and concluding remarks are given in Sec. VI.

II. EXPERIMENT

A. Apparatus

Experiments are carried out using the dynamic fluid-film interferometer (DFI), a custom-built apparatus [37]. The DFI, shown in Fig. 1(a), was slightly modified from that which is described in [37] to better accommodate experiments with solid substrates. The setup consists primarily of a Delrin chamber, which is filled with a silicone fluid. A spherical UV-fused silica planoconvex lens

TABLE I. Physical properties of silicone oils. The kinematic viscosity ν, dynamic viscosity μ, density ρ, surface tension γ, and refractive index n are obtained from data sheets supplied by the manufacturer (at 25 °C). The evaporative velocity E was measured at liquid temperatures of 27 °C.

ν (cSt)	μ [kg/(m s)]	ρ (kg/m^3)	γ (mN/m)	n	E (μm/s)	Supplier
0.65	0.49	760	15.9	1.375	1.3	ShinEtsu DM-Fluid
1.00	0.82	818	16.9	1.382	0.13	ShinEtsu DM-Fluid
1.50	1.28	852	17.7	1.387	0.023	ShinEtsu DM-Fluid
5.00	4.58	915	19.7	1.396	0.0001	Clearco PSF
10.0	9.35	935	20.1	1.399	–	Clearco PSF

with a radius of curvature of $a = 7.6$ mm (Lattice Electro Optics UF-PX-12.5-15-532) was chosen as the substrate material in order to prevent the oleic film from dewetting.

The substrate is initially held in place in the dome holder and the desired solution is pipetted into the chamber. A motorized actuator (Newport TRA12PPD) vertically positions the chamber relative to the substrate. In order to locate the air-liquid interface (the $z = 0$ plane), the chamber is lowered in small increments at a velocity of 0.15 mm/s, bringing the substrate closer to the free surface. Interference patters start to appear at the interface when the dome apex lies less than 4 μm below the interface. This vertical position is taken as $z = 0$. The chamber is then raised until the dome apex is submerged in the liquid at a distance of $b = 0.3$ mm below the planar air-liquid interface. The dome remains in place for 20 s, during which the user begins recording the video. At time $t = 0$ s, the motor lowers the chamber by 0.35 mm at a velocity of $U = 0.05$ mm/s, until the substrate apex comes to rest 50 μm above the $z = 0$ plane (a total transit time of $t^* = 7$ s). A procedural exception is made for the most volatile solvent (0.65 cSt; see Table I), wherein the chamber is initially lowered by a distance of 0.33 mm to offset evaporative losses incurred during the 20-s waiting period. The chamber is subsequently held in a fixed position for the remainder of the experiment. Further details on the experimental protocol can be found in the Supplemental Material [38].

As the substrate penetrates through the air-liquid interface, it captures a thin liquid film [Fig. 1(b)]. The interface is illuminated with a light source (CCS Inc. LAV-80SW2) and photographed with a camera (Imaging Development Systems UI-3080CP). If the film thickness falls below $\sim$10 μm, reflection interference leads to observable color patterns (see the Supplemental Material [38] for representative videos). These data can be used to calculate the thickness of the interstitial fluid between the solid substrate and the air-liquid interface within a 15-nm range of uncertainty [Fig. 1(b)]. However, reflections from the glass substrate's surface only allow us to accurately determine film thicknesses above 90 nm. A cover with acrylic sidewalls is placed around the entire setup to minimize film thickness fluctuations associated with sporadic convection in the upper air phase. The cover has a mesh top to allow for evaporation throughout the course of the experiment.

In order to determine the minimum film thickness deposited over the glass substrate, additional experiments were conducted for pure silicone oils using ellipsometry (Horiba UVISEL Spectroscopic Phase Modulated Ellipsometer), an optical technique that measures the change in polarization of light as it reflects and transmits through different layers of a stratified sample. In these experiments, the spherical UV-fused silica substrate was entirely submerged in a bath of pure volatile silicone oil; the glass substrate was cleaned with acetone and plasma treated (Diener Pico oxygen plasma cleaner) prior to all ellipsometric measurements. Some of this oil was then pipetted out until the top surface of the lens was exposed to the air, capturing a microscopic film of oil that was allowed to evaporate to nanoscopic dimensions. The bottom portion of the lens remained submerged in the oil bath, providing a bulk fluid reservoir and mimicking the experimental conditions of the DFI. The thickness of the captured oil film was determined from the difference

between measurements before and after immersion in the silicone oil. Sample ellipsometric data are presented in the Supplemental Material [38].

B. Silicone-oil mixtures

Binary mixtures of low-molecular-weight silicone oils (polydimethylsiloxane) are chosen as model liquids due to their good chemical stability and Newtonian behavior. During an experiment, the temperature of the silicone oils was measured to be 27 °C. This measurement is slightly higher than room temperature due to the radiant heat generated by the light source (the light intensity was not varied throughout all experiments). A thermal camera [FLIR T650sc with close-up IR lens, 5.8× (100 μm)] was used to show that temperature variations at the liquid-air interface, which can potentially induce undesired thermocapillary flows, are absent (see [39] and the Supplemental Material [38] for thermocapillary data).

Some relevant physical properties of the silicone oils are presented in Table I. Important material properties, including the kinematic viscosity ν, dynamic viscosity μ, density ρ, surface tension γ, and refractive index n, are obtained from data sheets provided by the supplier. The refractive index of the volatile component was used for all film thickness calculations, since changes in n caused by concentration variations have a negligible effect on the calculated film thicknesses. A human error of $\pm$15 nm (for films thicker than 100 nm) has been previously estimated by Frostad *et al.* based on the minimum band spacing in the interpreted color interference pattern [37].

In order to characterize the volatility of each oil, separate measurements are performed (see the Supplemental Material [38] for evaporation data). The Delrin chamber was filled with a pure oil and exposed to the light source. The total liquid mass was recorded as a function of time, from which the total mass flux (per unit area of free surface) was calculated. By dividing the measured mass flux by the liquid density, the volumetric flux per unit area E was computed. This quantity is reported in Table I for different oils. For the liquids studied, an increase in solvent viscosity of 0.5 cSt approximately corresponds to an order of magnitude reduction in the evaporative velocity.

Three different binary liquid mixtures consisting of a volatile solvent (ShinEtsu DM-Fluid) and a nonvolatile solute (Clearco PSF) are used in the experiments. As is common practice in industry, each silicone oil will be hereafter identified using the value of its kinematic viscosity (in units of centistokes). The solvent-solute pairs used in the experiments are 0.65 cSt/5.00 cSt, 1.00 cSt/5.00 cSt, and 1.50 cSt/10.0 cSt. The bulk volume fraction of the solute species is denoted by ϕ_∞ and is varied in the range 0.01%–0.50%. Evaporation-driven solutocapillary flows are studied by varying ϕ_∞ (by changing the fraction of the high-molecular-weight species in the mixture) and E (by exchanging out the solvent) in the experiments. Increasing ϕ_∞ has the effect of enhancing Marangoni stresses induced by gradients in surface tension, whereas E controls the rate of evaporation.

III. THEORY

A. Governing equations

A model for the spatiotemporal evolution of the evaporating liquid film over a curved substrate is formulated under the auspices of lubrication theory. A schematic of the model geometry, consisting of a solid sphere of radius $a = 7.6$ mm submerged in a binary liquid mixture with a free surface, is shown in Fig. 2. The origin is positioned in the plane of the undeformed free surface, directly above the sphere's center. A cylindrical coordinate system (r, θ, z) is adopted, where r is the radial distance from the centerline, θ is the azimuthal angle, and z is the axial distance from the undeformed plane. Gravity points in the $-z$ direction and has acceleration $g = 9.8\,\mathrm{m/s^2}$. In order to replicate the experiment, the position of the sphere apex $z = -h_s(t)$ is advanced in a ramp-hold sequence,

$$h_s(t) = b - U[t - (t - t^*)H(t - t^*)], \tag{1}$$

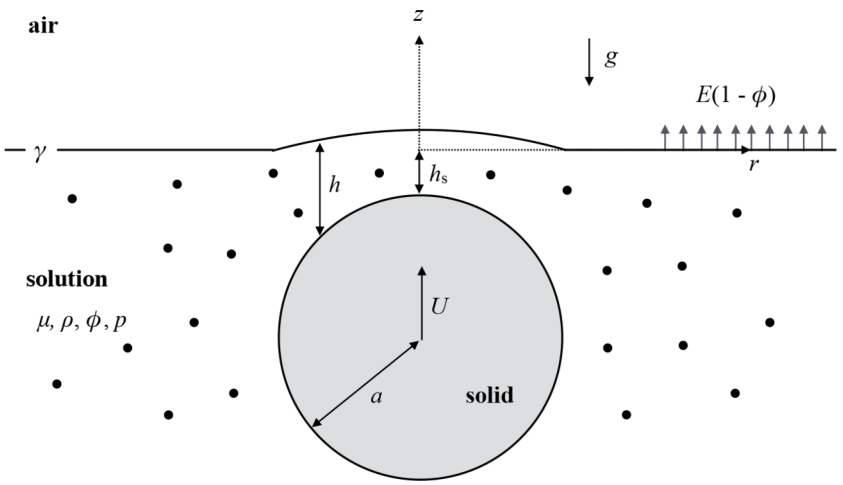

FIG. 2. Schematic of the model geometry.

where $b = 0.3$ mm, $U = 0.05$ mm/s, $t^* = 7$ s, and $H(t)$ is the unit step function. At times $t < 0$, the apex of the sphere is held fixed at a vertical height $z = -b$. At $t = 0$, the sphere translates upward with constant velocity U. The film thins through the translation until the sphere apex reaches its final position $z = Ut^* - b$ at $t = t^*$, after which thinning continues as the solvent evaporates with characteristic flux E.

In the experiments, the substrate translates slowly relative to the timescale of free-surface shape relaxation, i.e., the capillary number $\mathrm{Ca} = \mu U/\gamma_0$, calculated using the solvent viscosity μ and surface tension γ_0, is typically of $O(10^{-6})$ (see Table II). Consequently, the thickness of the film that is captured at $t = t^*$ is small compared to the initial separation b. Our numerical calculations indicate that the thickness of this captured film scales with $a\sqrt{\mathrm{Ca}}$, in agreement with scaling arguments made by Frostad *et al.* [37]. We therefore define the characteristic captured-film thickness as $h^* = a\sqrt{\mathrm{Ca}}$. Crucially, lubrication theory is expected to give a good approximation of the flow physics for times $t \geqslant 0$ so long as the ratios b/a and $h^*/a = \sqrt{\mathrm{Ca}}$ are *both* small compared to unity (in our experiments, $b/a = 0.04$ and $h^*/a = 0.001$-0.002).

We assume that the system remains rotationally symmetric about the z axis, so gradients with respect to θ may be neglected. Under the lubrication approximation, the evolution of the film

TABLE II. Values of the dimensionless parameters used in the experiments, tabulated for different silicone-oil mixtures (see Table I for oil properties). In all experiments, $a = 7.6$ mm, $b = 0.3$ mm, and $U = 0.05$ mm/s. The species diffusivity is estimated to be $D \simeq 10^{-10}$ m^2/s. The Hamaker constant is estimated to be $A \simeq 10^{-19}$ J.

Solvent-solute pair	0.65 cSt 5.00 cSt	1.00 cSt 5.00 cSt	1.50 cSt 10.0 cSt
Ca	1.6×10^{-6}	2.4×10^{-6}	3.6×10^{-6}
Bo	3.4×10^{-2}	4.3×10^{-2}	5.2×10^{-2}
Ha	$\sim 10^{-6}$	$\sim 10^{-6}$	$\sim 10^{-6}$
Pe	$\sim 10^{3}$	$\sim 10^{3}$	$\sim 10^{3}$
Ma/ϕ_∞	1.9×10^{2}	1.1×10^{2}	7.1×10^{1}
Ev	2.6×10^{-2}	2.6×10^{-3}	4.6×10^{-4}

thickness $h(r,t)$ and solute-species concentration $\phi(r,t)$ is governed by the local mass balance

$$\frac{\partial h}{\partial t}+\frac{1}{r}\frac{\partial}{\partial r}\left[rh\left(\frac{h}{2\mu}\frac{\partial \gamma}{\partial r}-\frac{h^2}{3\mu}\frac{\partial p}{\partial r}\right)\right]=-E(1-\phi) \tag{2}$$

and species mass balance

$$\frac{\partial (h\phi)}{\partial t}+\frac{1}{r}\frac{\partial}{\partial r}\left[rh\phi\left(\frac{h}{2\mu}\frac{\partial \gamma}{\partial r}-\frac{h^2}{3\mu}\frac{\partial p}{\partial r}-D\frac{\partial \ln \phi}{\partial r}\right)\right]=0, \tag{3}$$

where μ is the solvent viscosity, D is the solute-species diffusivity, $\gamma(r,t)$ is the surface tension, and $p(r,t)$ is the dynamic pressure. Under isothermal conditions, the surface tension is solely a function of the chemical composition of the free surface. We assume here that γ is related to ϕ by the simple linear law

$$\gamma=\gamma_0+(\gamma_1-\gamma_0)\phi, \tag{4}$$

where γ_0 and γ_1 are the surface tensions of the pure solvent ($\phi=0$) and pure solute ($\phi=1$), respectively. Thus, γ can be eliminated from the previous equations by use of (4). A balance of normal stresses at the upper free surface yields the expression for the pressure

$$p=\gamma_0\left[\frac{2}{a}-\frac{1}{r}\frac{\partial}{\partial r}\left(r\frac{\partial h}{\partial r}\right)\right]+\rho g(h-h_\infty)-\frac{A}{6\pi h^3}, \tag{5}$$

where ρ is the solvent density, A is the Hamaker constant, and

$$h_\infty(r,t)=h_s(t)+\frac{r^2}{2a}-E(1-\phi_\infty)t \tag{6}$$

is the parabolic approximation of the film thickness in the far field [recall that h_s is given by (1)]. Here the far field corresponds to the bulk fluid region where the depth is large compared to the thin-film region. In Eq. (5) we have approximated the London–van der Waals force by a disjoining pressure acting on the upper free surface, $\Pi=-A/6\pi h^3$. This expression applies to nonionic liquid films with thicknesses $\gtrsim$10 Å resting atop high-energy surfaces, such as glass [26,31,32,40]. The initial and boundary conditions for (2), (3), and (5) are

$$h=h_\infty,\quad \phi=\phi_\infty \quad \text{at } t=0, \tag{7a}$$

$$\frac{\partial h}{\partial r}=0,\quad \frac{\partial \phi}{\partial r}=0,\quad \frac{\partial p}{\partial r}=0 \quad \text{at } r=0, \tag{7b}$$

$$h=h_\infty,\quad \phi=\phi_\infty,\quad p=0 \quad \text{as } r\to\infty. \tag{7c}$$

A complete derivation of the preceding equations can be found in the Supplemental Material [38].

Some discussion of the physical meaning of the terms appearing in Eqs. (2)–(5) are in order. Solvent evaporation, which appears as a sink on the right-hand side of (2), concentrates the solute ϕ at a rate $E(1-\phi)/h$. The normal stress balance (5) prescribes the dynamic pressure p in the liquid, which contains contributions due to capillarity, gravity, and van der Waals forces. Capillary forces play a role wherever there are variations in surface curvature, which naturally appear in this geometry (the free surface conforms to the curvature of the substrate near the centerline, whereas it flattens in the far field). Gravitational forces (modulated by the force density ρg) are necessary to weigh down the surface in the far field, or else the shape of the free surface would not be bounded [41]. However, gravity plays a comparably weaker role (relative to capillarity and van der Waals forces) in the vicinity of the centerline, where the film is much thinner. For the air–silicone oil–glass system, the Hamaker constant A is positive and the resulting disjoining pressure Π is negative, which has the effect of drawing fluid into films that become precipitously thin. A positively valued Hamaker constant $A>0$ corresponds to complete wetting of the substrate by the liquid film,

denoting a repulsive interaction between the substrate and the free surface. Thus, London–van der Waals forces act to stabilize the film, preventing the onset of dewetting. The terms appearing inside the large parentheses in Eqs. (2) and (3) have units of a volumetric flux per unit distance. The pressure flux $-(h^2/3\mu)(\partial p/\partial r)$, Marangoni flux $(h/2\mu)(\partial\gamma/\partial r)$, and diffusive flux $-D(\partial \ln\phi/\partial r)$ compete in advecting the total volume per unit area of solvent $(1-\phi)h$ and solute ϕh.

At this point, it behooves us to address some of the simplifying assumptions made in the above model. First, we have assumed a rather simple evaporation model where the rate of evaporation $-E(1-\phi)$ depends linearly on the solvent volume fraction with a constant coefficient. A more sophisticated (albeit more complicated) model would consider the coupled transport of the volatile species in both the liquid and vapor phases, from which the rate of evaporation is calculated from the concentration profiles at the free surface. Second, we have approximated the density and viscosity of the mixture by the solvent properties ρ and μ, respectively, which precludes the possibility of spatial variations in density and viscosity induced by concentration inhomogeneities. Even though prior work has examined the dependence of viscosity on mixture composition [4,6,7], we have decided to neglect these contributions and exclusively focus on the effects of changing $\phi(r,t)$ on the Marangoni flux. We have similarly assumed the surface tension γ to be well approximated by γ_0 in the first term on the right-hand side of (5). These approximations are expected to be valid at dilute solute concentrations $\phi \ll 1$. Third, the simple mixture rule (4) does not necessarily give an accurate measure of the true variation in γ with respect to changes in ϕ; it only provides a linear interpolation between the two limiting values at $\phi = 0$ and 1. This linearized relationship is commonly used in the literature [3,4,15,17] and captures the leading-order effects induced by changes in surface tension. Finally, we have incorporated species diffusion and intermolecular forces by introducing the additional parameters D and A, which are not known and must be estimated. Despite these simplifications, the initial-boundary-value problem (2)–(7) includes contributions from evaporation, Marangoni stresses, species diffusion, capillarity, gravity, and intermolecular forces in the coupled nonlinear transport of $h(r,t)$, $\phi(r,t)$, and $p(r,t)$. Thus, we expect the model to *qualitatively* capture physical phenomena observed in the experiments.

B. Scalings and dimensionless parameters

The preceding equations are cast into dimensionless form through a proper choice of characteristic concentration, length, velocity, and pressure scales. The obvious choice for a concentration scale is ϕ_∞, the bulk solute volume fraction. Since we are most interested in the film dynamics after cessation of the sphere's motion ($t \geqslant t^*$), the captured-film thickness $h^* = a\sqrt{\mathrm{Ca}} = a\sqrt{\mu U/\gamma_0}$ is a natural choice of transverse (axial) length scale. The associated lateral (radial) length scale is $\sqrt{ah^*}$, chosen based on the curvature of the substrate so that the lubrication approximation is strictly valid in the region where $r = O(\sqrt{ah^*})$. Balancing the pressure with the capillary stress in Eq. (5) then yields γ_0/a as a characteristic pressure scale. Finally, lubrication theory yields $(h^*)^3(\gamma_0/a)/\mu a h^* = U$ as the (axial) velocity scale. Interestingly, the substrate velocity U emerges as the proper velocity scale in spite of the fact that the motion of the substrate ceases after $t = t^*$. This is a direct consequence of the fact that the captured-film thickness h^* depends on the rate at which the substrate penetrates the $z = 0$ plane.

Using the aforementioned scales, we introduce the dimensionless variables

$$\bar{\phi} = \frac{\phi}{\phi_\infty}, \quad \bar{h} = \frac{h}{h^*} = \frac{h}{a\sqrt{\mathrm{Ca}}}, \quad \bar{r} = \frac{r}{\sqrt{ah^*}} = \frac{r}{a\mathrm{Ca}^{1/4}},$$
$$\bar{p} = \frac{h^{*2}p}{\mu U a} = \frac{ap}{\gamma_0}, \quad \bar{t} = \frac{Ut}{h^*} = \frac{\sqrt{\mathrm{Ca}}\gamma_0 t}{\mu a}, \tag{8}$$

where we have eliminated $h^* = a\sqrt{\mathrm{Ca}}$ in favor of the capillary number $\mathrm{Ca} = \mu U/\gamma_0$, which contains the dependence on the substrate velocity U. By introducing (8) into (1)–(7), we obtain

the *dimensionless* equations

$$\frac{\partial \bar{h}}{\partial \bar{t}} + \frac{1}{\bar{r}}\frac{\partial}{\partial \bar{r}}\left[\bar{r}\bar{h}\left(\frac{\mathrm{Ma}\bar{h}}{2}\frac{\partial \bar{\phi}}{\partial \bar{r}} - \frac{\bar{h}^2}{3}\frac{\partial \bar{p}}{\partial \bar{r}}\right)\right] = -\mathrm{Ev}(1-\phi_\infty\bar{\phi}), \tag{9}$$

$$\frac{\partial(\overline{h\phi})}{\partial \bar{t}} + \frac{1}{\bar{r}}\frac{\partial}{\partial \bar{r}}\left[\bar{r}\overline{h\phi}\left(\frac{\mathrm{Ma}\bar{h}}{2}\frac{\partial \bar{\phi}}{\partial \bar{r}} - \frac{\bar{h}^2}{3}\frac{\partial \bar{p}}{\partial \bar{r}} - \frac{1}{\mathrm{Pe}}\frac{\partial \ln \bar{\phi}}{\partial \bar{r}}\right)\right] = 0, \tag{10}$$

$$\bar{p} = 2 - \frac{1}{\bar{r}}\frac{\partial}{\partial \bar{r}}\left(\bar{r}\frac{\partial \bar{h}}{\partial \bar{r}}\right) + \mathrm{Bo}(\bar{h} - \bar{h}_\infty) - \frac{\mathrm{Ha}}{\bar{h}^3}, \tag{11}$$

with

$$\bar{h} = \bar{h}_\infty, \quad \bar{\phi} = 1 \quad \text{at } \bar{t} = 0, \tag{12a}$$

$$\frac{\partial \bar{h}}{\partial \bar{r}} = 0, \quad \frac{\partial \bar{\phi}}{\partial \bar{r}} = 0, \quad \frac{\partial \bar{p}}{\partial \bar{r}} = 0 \quad \text{at } \bar{r} = 0, \tag{12b}$$

$$\bar{h} = \bar{h}_\infty, \quad \bar{\phi} = 1, \quad \bar{p} = 0 \quad \text{as } \bar{r} \to \infty, \tag{12c}$$

where

$$\bar{h}_\infty(\bar{r}, \bar{t}) = \bar{b} - \bar{t} + (\bar{t} - \bar{t}^*)H(\bar{t} - \bar{t}^*) + \frac{\bar{r}^2}{2} - \mathrm{Ev}(1-\phi_\infty)\bar{t}, \tag{13}$$

with $\bar{b} = b/a\sqrt{\mathrm{Ca}}$ and $\bar{t}^* = \sqrt{\mathrm{Ca}}\gamma_0 t^*/\mu a$. In Eqs. (9)–(13) we have introduced the following dimensionless parameters:

$$\mathrm{Ca} = \frac{\mu U}{\gamma_0} \quad \text{(capillary number)}, \tag{14a}$$

$$\mathrm{Bo} = \frac{\rho g a h^*}{\gamma_0} = \frac{\rho g a^2\sqrt{\mathrm{Ca}}}{\gamma_0} \quad \text{(Bond number)}, \tag{14b}$$

$$\mathrm{Ha} = \frac{Aa}{6\pi h^{*3}\gamma_0} = \frac{A}{6\pi a^2 \mathrm{Ca}^{3/2}\gamma_0} \quad \text{(dimensionless Hamaker constant)}, \tag{14c}$$

$$\mathrm{Pe} = \frac{Ua}{D} \quad \text{(Péclet number)}, \tag{14d}$$

$$\mathrm{Ma} = \frac{\phi_\infty(\gamma_1 - \gamma_0)h^*}{\mu U a} = \frac{\phi_\infty(\gamma_1 - \gamma_0)\sqrt{\mathrm{Ca}}}{\mu U} \quad \text{(Marangoni number)}, \tag{14e}$$

$$\mathrm{Ev} = \frac{E}{U} \quad \text{(dimensionless evaporative velocity)}. \tag{14f}$$

A description of the physical meaning of the dimensionless groups (14) is in order. The capillary number Ca defines the ratio of viscous stresses to capillary (i.e., surface-tension) stresses and thus gauges the ability of the free surface to deform in response to the motion of the substrate. The Bond number Bo is the square of the ratio between the characteristic radial length scale $\sqrt{ah^*}$ and the capillary length $\sqrt{\gamma_0/\rho g}$, which in turn sets the distance from the centerline at which gravitational forces become relevant to surface deformation. The dimensionless Hamaker constant Ha quantifies the importance of van der Waals forces (relative to capillary forces) in stabilizing the liquid film from rupture. The Péclet number Pe gauges the relative rates of species advection and diffusion. The Marangoni number Ma is the ratio between solutocapillary stresses induced by surface-tension gradients and viscous stresses induced by fluid flow. Finally, the dimensionless evaporative velocity Ev gauges the relative rates of evaporation and the lateral fluid flux.

Values of the dimensionless parameters (14) used in the experiments are reported in Table II. The parameters a, b, U, μ, ρ, γ_0, γ_1, E, and ϕ_∞ are either measured or controlled in the experiments

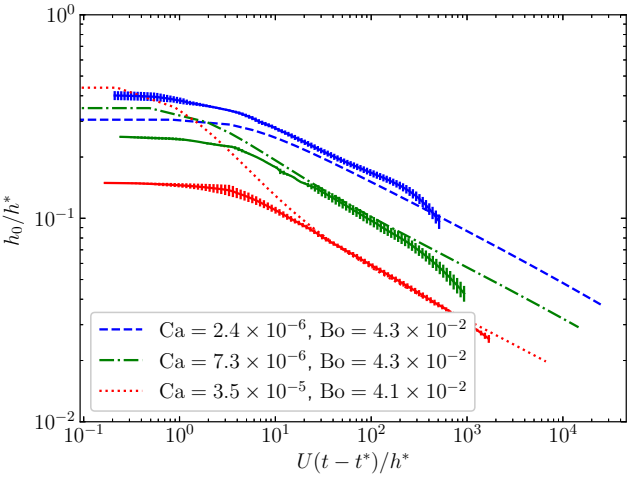

FIG. 3. Comparison of the numerical computations (dashed lines) to experimental measurements (solid lines) for pure silicone fluids in the absence of evaporation. Lines and error bars in the experimental data represent the mean and standard deviation, respectively, of repeated measurements (duplicates or triplicates). The blue data are for ν=1 cSt, U=0.05 mm/s, t^*=7 s, and b=0.3 mm; green data for ν=1 cSt, $U = 0.15$ mm/s, $t^* = 2.3$ s, and $b = 0.3$ mm; and red data for $\nu = 5$ cSt, $U = 0.15$ mm/s, $t^* = 2.3$ s, and $b = 0.3$ mm.

(see Sec. I). The other parameters D and A are estimated based on previous literature. The species diffusivity $D \simeq 10^{-10}$ m^2/s is extrapolated from data for different high-viscosity silicone oil mixtures [42]. Separately performed ellipsometry measurements indicate that the minimum film thickness lies in the range 10–20 Å for pure evaporating 1.00-cSt silicone oils (see the Supplemental Material [38]). For disjoining pressures dominated by van der Waals forces and taking into consideration the approximate molecular sizes of our silicone oils, the Hamaker constant for our system is estimated to be approximately $A \simeq 10^{-19}$ J [26,40].

C. Numerical method

Equations (9)–(12) are integrated numerically using the finite-difference method. Equation (10) is weakly parabolic at large Pe. As such, special care must be taken in the discretization of this equation so as to avoid numerical instabilities associated with sharp gradients in $\overline{\phi}$. We found that solving for $\overline{g} = \ln \overline{\phi}$ instead of $\overline{\phi}$ removes such instabilities. This approach was inspired in part by theoretical progress in other fields, including turbulence [43] and flow of polymeric liquids [44,45].

The nonlinear partial differential equations (9)–(11) are first linearized and subsequently discretized onto a radial grid. A coordinate transformation is used in order to cluster grid points near $\overline{r} = 0$. Partial derivatives with respect to $\overline{r}$ are replaced by second-order accurate difference analogs; time advancement is carried out using a Crank-Nicolson scheme with adaptive control of the step size. At each time level, the linearized equations form a bipentadiagonal system, which can be efficiently solved by direct elimination. Newton iteration is carried out until the solution converges (a typical tolerance is the square of the time step size). Verification tests were performed to ensure that the model reproduced analytical solutions in the small deformation limit ($a^2\mathrm{Ca}/b^2 \ll 1$) (see [46] and the Supplemental Material [38] for additional details on the numerical method and the small deformation analysis).

The numerical model was validated against experiments with pure silicone oils. Evaporation was suppressed by placing a glass cover directly over the Delrin chamber. In this simplified system, the model reduces to the solution of (9) and (11) for the film thickness $\overline{h}(\overline{r}, \overline{t})$ with $\overline{\phi} = 0$. The substrate velocity was varied from $U = 0.05$ to 0.15 mm/s to obtain a range of Ca. Figure 3 shows

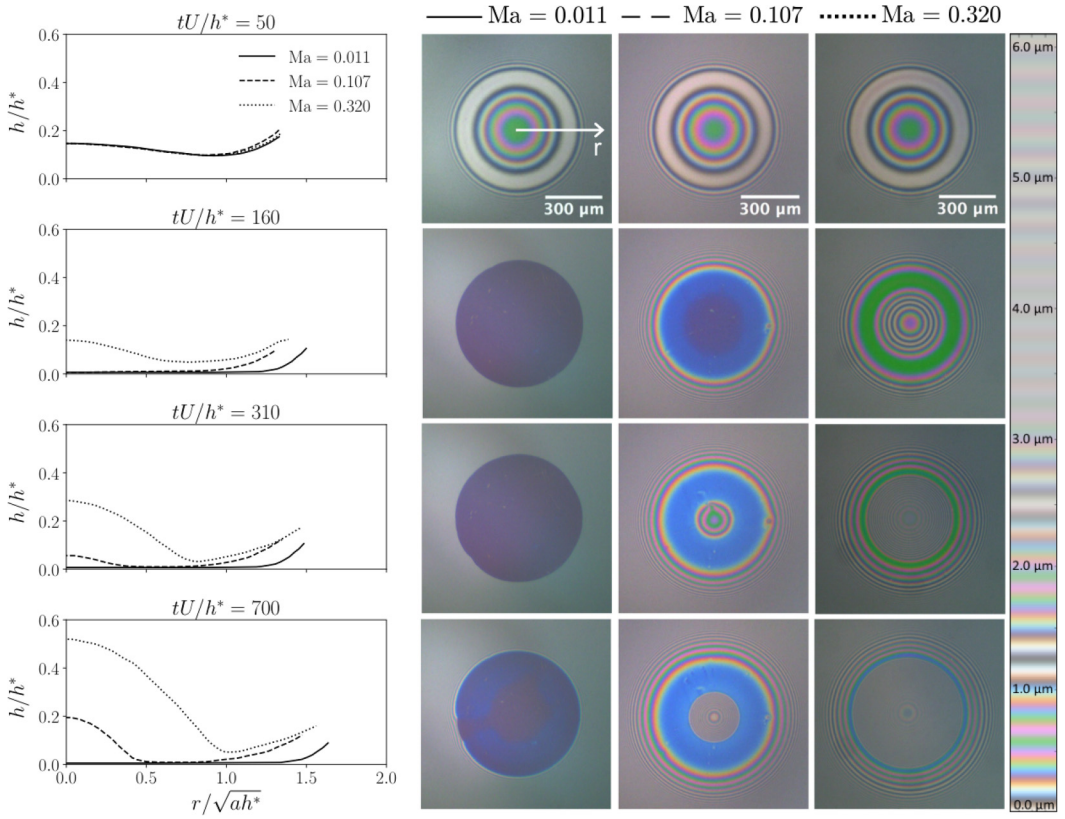

FIG. 4. Time series of experimental film thickness profiles are plotted for 1.00 cSt/5.00 cSt blends (Ev = 2.6×10^{-3}) at Ma = 0.011 ($\phi_\infty = 0.01\%$), Ma = 0.107 ($\phi_\infty = 0.10\%$), and Ma = 0.320 ($\phi_\infty = 0.30\%$), as determined experimentally. Snapshots of the interferometric patterns, viewed from the top camera, are shown at the corresponding times and compositions. Experiments show the presence of three distinct flow regimes: the van der Waals regime (solid line), the intermediate regime (dashed line), and the capillary regime (dotted line).

a plot of the centerline film thickness $\overline{h}_0 \equiv \overline{h}(0, \overline{t})$ for three parameter sets, wherein quantitative agreement between the experiments and theory was achieved at long times. At short times, there is a discrepancy in the initial film thickness, due to difficulty in interpreting interference patterns at large thicknesses.

IV. RESULTS

Below we present our experimental and theoretical results. Our main objective is to determine the effects of varying the solute concentration (i.e., the Marangoni number Ma) and solvent volatility (i.e., the dimensionless evaporative velocity Ev) on the thin-film dynamics.

A. Film profiles

Figure 4 shows experimental measurements of the dimensionless film thickness $\overline{h} = h/h^*$ plotted against the dimensionless radius $\overline{r} = r/\sqrt{ah^*}$ at different time points $\overline{t} = tU/h^* = 50$, 160, 310, and 700, along with the corresponding interferometric patterns. The measurements were obtained using a 1.00 cSt/5.00 cSt mixture (Ev = 2.6×10^{-3}) at three different solute concentrations (Ma = 0.011, 0.107, and 0.320). Only axisymmetric profiles are observed in the experiments. Azimuthal instabilities were not observed, although it is well known that problems related to the spreading

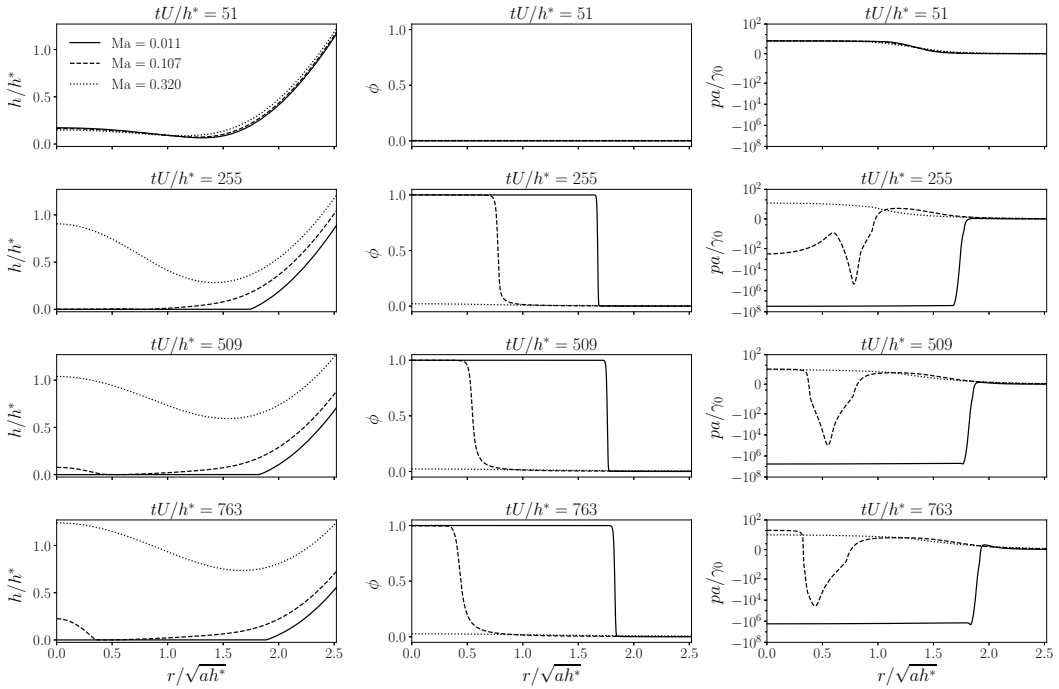

FIG. 5. Time series of the dimensionless film thickness $\overline{h}(\overline{r},\overline{t})$, solute concentration $\phi(\overline{r},\overline{t})$, and dimensionless dynamic pressure $\overline{p}(\overline{r},\overline{t})$ profiles at three different Marangoni numbers Ma = 0.011 ($\phi_\infty = 0.01\%$), Ma = 0.107 ($\phi_\infty = 0.10\%$), and Ma = 0.320 ($\phi_\infty = 0.30\%$), as determined theoretically. The other dimensionless parameters used in the numerical calculations are Ca = 2.4×10^{-6}, Pe = 10^3, Bo = 4.3×10^{-2}, Ha = 1.6×10^{-6}, and Ev = 2.6×10^{-3}.

of thin films due to surface-tension gradients are often susceptible to hydrodynamic instabilities [18–20,47–51]. Asymmetries are only observed at higher Ma or when the rate of solvent evaporation is instantaneously suppressed (see the Supplemental Material [38] for examples of instabilities observed).

Figure 5 shows theoretical predictions of the dimensionless film thickness $\overline{h}$, solute concentration ϕ, and dimensionless dynamic pressure $\overline{p} = ap/\gamma_0$ for the same parameters shown in Fig. 4. Many of the same features observed in the experimentally measured film-thickness profiles are reproduced in Fig. 5. The measured and simulated profiles elucidate three distinct regimes of flow. Namely, at low Ma (van der Waals regime) the film thins to nanoscopic dimensions and remains nearly uniform; at intermediate Ma (intermediate regime), a mound forms at the centerline, surrounded by a nanoscopic fluid layer, and grows over time; at high Ma (capillary regime), the film remains microscopically thick and grows over time. Further details regarding the three regimes are provided in Secs. IV A 1–IV A 3 below.

Additional experiments were conducted with 0.65- and 1.50-cSt solvents (see the Supplemental Material [38] for representative videos). Varying the rate of evaporation changes the range of Ma where each of the three regimes is observed. Most notably, it was observed that incrementing the rate of evaporation broadens the range of Ma in the intermediate regime, where a viscous mound is stabilized by a nanoscopically thin film. We hypothesize that this occurs because the timescale of solvent depletion due to evaporation becomes smaller compared to the diffusive timescale ($\mathrm{Pe}^{-1} \ll \mathrm{Ev}$), attenuating the effects of diffusion in homogenizing concentration gradients. Larger values of Ev also lead to more rapid fluid depletion, which ensures that a nanoscopic film will be present at higher Ma.

1. van der Waals regime: Evaporation to a nanoscopic film

At low Ma (Ma = 0.011 in Figs. 4 and 5), the liquid evaporates and forms a nearly uniform film of nanoscopic dimensions, but never dewets the substrate (dark blue color in Fig. 4). van der Waals forces are expected to play a significant role in this region due to the small separation between the substrate and free surface. A weak, radially inward flux draws fluid towards the centerline, which stabilizes the film.

Ellipsometric measurements reveal that the thickness of the nanoscopic film lies between 10 and 20 Å for a pure 1.00-cSt silicone oil. These results confirm that the thin fluid film present in the van der Waals regime is still subject to long-range forces and that modeling these interactions via a disjoining pressure of the form given in Eq. (5) is an acceptable approximation. If the film thins to molecular dimensions ($\lesssim$ 10 Å), short-range interactions such as steric effects come into play and quantitative formulas for these interactions are unavailable [31,40].

The coupled evolution of ϕ and $\overline{p}$ in Fig. 5 elucidates the dominant driving forces during film evolution. At Ma = 0.011 in Fig. 5, evaporation of the low-molecular-weight solvent enriches the high-molecular-weight solute near the centerline ($\phi = 1$ at later times). Solute concentration gradients become very steep within a narrow transition region separating the thin film from the bulk. Despite these steep gradients, the Marangoni flux $\mathrm{Ma}(\overline{h}/2)(\partial\overline{\phi}/\partial\overline{r})$ is relatively weak due to the smallness of $\overline{h}$; solutocapillary forces alone are not responsible for stabilizing the film. Concomitantly, the dimensionless pressure $\overline{p}$ drops to negative values in the thin-film region (where $\overline{h}$ nearly vanishes), indicating a strong disjoining pressure due to the intermolecular interaction between the substrate and the free surface. The pressure flux due to intermolecular forces $-(\mathrm{Ha}/\overline{h}^2)(\partial\overline{h}/\partial\overline{r})$, which scales inversely with $\overline{h}^2$, is large compared to the aforementioned Marangoni flux, indicating that disjoining pressure is responsible for stabilizing the film at low Ma. At long times, the theory predicts a dimensional apical thickness of 5 nm for Ma = 0.011. This value is in agreement with the nanoscopic film thickness as measured via ellipsometry.

2. Intermediate regime: Formation of a solute-rich mound stabilized by a nanoscopic film

At intermediate Ma (Ma = 0.107 in Figs. 4 and 5), the film initially evaporates and forms a nanoscopic layer of thickness comparable to that in the van der Waals regime. After some time ($\bar{t}$ = 300–500), a viscous mound (microns in thickness) forms at the centerline above the substrate apex, surrounded by a nanoscopically thin fluid layer about 150 μm wide. The thickness of this nanoscopic layer increases from about 10–20 Å prior to mound formation to $\simeq$100 nm after mound formation, as evidenced in the change in color from dark to lighter blue in Fig. 4. The mound continues to grow in height and volume over time.

As Ma is increased, solute enrichment near $\overline{r} = 0$ is diminished and different contributions to the dimensionless pressure $\overline{p}$ come into play. Namely, positive pressures ($\overline{p} > 0$) indicate strong capillary forces, whereas negative pressures ($\overline{p} < 0$) indicate strong intermolecular forces. On examining the intermediate-Ma case (Ma = 0.107 in Fig. 5), it is apparent that the formation of a microscopically thick mound results in a locally dominant capillary pressure (gravity is comparably weak). This result is corroborated by our experiments, in which the observed mounds have a spherical-cap geometry. In the thin-fluid layer surrounding the mound, disjoining pressure dominates. The pressure flux forcing fluid out of the (solute-enriched) mound and into the (solute-depleted) thin-fluid layer is offset by the Marangoni flux drawing fluid inward, due to the gradient in the solute concentration. Consequently, the mound volume grows as a function of time.

3. Capillary regime: Rapid film regeneration

At high Ma (Ma = 0.320 in Figs. 4 and 5), the mixture contains a higher fraction of the nonvolatile component and solutocapillary flows are induced at earlier times. Consequently, the film does not have enough time to deplete to form a nanoscopic layer. Fluid is continuously regenerated to the film and the solute-enriched mound [defined as the region between the apex at $r = 0$ and the

location of minimum film thickness R at $h(R,t) = h_{\min}$] forms as a result of the balance between Marangoni and capillary forces. Moreover, the rate of film thickening is much higher than at lower Ma (about a twofold increase between Ma = 0.107 and 0.320). Referring to the simulations in Fig. 5, the pressure is completely dominated by the capillary contribution, which results in a qualitatively different film profile. In this regime, the film profile resembles liquid drainage between two foam bubbles, wherein a dimple forms at the centerline and is surrounded by a barrier ring [52]. The theory overpredicts both the centerline film thickness $\bar{h}_0$ and minimum film thickness $\bar{h}_{\min}$ in this regime.

B. Growth rates

In this section we quantify the evolution of the centerline film thickness. Figures 6 and 7 show plots of the dimensionless centerline film thickness $\bar{h}_0 = h(0,t)/h^*$ as a function of dimensionless time $\bar{t}$, as determined via experiment and theory, respectively. The experiments were performed using a 1.00 cSt/5.00 cSt mixture (the same solvent-solute combination reported in Fig. 4) over a range of solute concentrations, resulting in a fixed evaporation rate (Ev $= 2.6 \times 10^{-3}$) and a range of Marangoni numbers (Ma = 0.021–0.320). Since the exact value of the Hamaker constant for our systems is unknown, the simulations were conducted at two different values of Ha in order to obtain a range of possible film thicknesses $\bar{h}_0$. It is important to emphasize that the experimental accuracy of the interferometer only allows us to determine film thicknesses within a 15-nm range of uncertainty [37]; consequently, dimensionless film thicknesses below $\bar{h} \simeq 7.5 \times 10^{-3}$ cannot be resolved in our measurements.

Both experiment and theory indicate that increasing Ma tends to increase the rate of film growth. The mechanism of acceleration was described in the preceding section: A higher Marangoni flux assists in the formation and stabilization of a solute-enriched mound bordered by a nanoscopically thin film. As Ma is increased further, the rate of growth of the solute-enriched mound increases and the nanoscopic film disappears. Similar trends were reported by Fanton and Cazabat, wherein increasing the concentration of a nonvolatile constituent in an evaporating mixture enhanced the propagation of a liquid front via solutocapillary flow [19].

Our numerical calculations indicate that at sufficiently high Ma (Ma = 0.213–0.320 in Fig. 7), the thin film bordering the mound begins to withdraw fluid from the mound at some point during film growth. For the cases Ma = 0.213, 0.266, and 0.320 shown in Fig. 7, fluid withdrawal occurs at $\bar{t} \simeq 590$, 350, and 250, respectively, whereupon the film grows at a slower rate due to enhanced capillary forces. This effect is not seen in the experiments reported in Fig. 7, wherein the thin film bordering the mound is maintained over the course of the experiment. We have performed additional experiments at higher values of Ma (given in the Supplemental Material [38]) and have observed fluid withdrawal from the mound into the bordering thin-film region. In these experiments, the sudden withdrawal induces a symmetry-breaking instability near the minimum film thickness $h_{\min}$, resulting in undulations in the film thickness around the perimeter of the mound. It is important to note that all experimental data shown in this paper correspond to *axisymmetric* profiles, prior to the development of any flow instability.

It is noteworthy that the growth curves shown in Fig. 7 collapse onto each other at high Ma, whence the growth of $\bar{h}_0$ becomes insensitive to changes in Ma and is mostly controlled by the rate of evaporation (Ev). This trend is observed in the experiments at high Ma (Fig. 6, Ma = 0.213, 0.266, and 0.320), wherein the growth rates are not strongly affected by changes in Ma. Quantitatively, the theoretical calculations slightly overpredict the centerline film thickness $\bar{h}_0$ when Ma is large, for the particular value of Ev reported in Figs. 6 and 7.

At lower Ma, the theory underpredicts the film growth rate and thickness (about an order of magnitude discrepancy in $\bar{h}_0$). In this van der Waals regime, the pressure profiles indicate a dominant disjoining-pressure contribution and the solute concentration ϕ is not small (see the Ma = 0.011 case in Fig. 5, where ϕ increases to unity near $\bar{r} = 0$). The modest film growth at low Ma, according to the theoretical predictions, is due entirely to a pressure gradient induced by van der Waals forces.

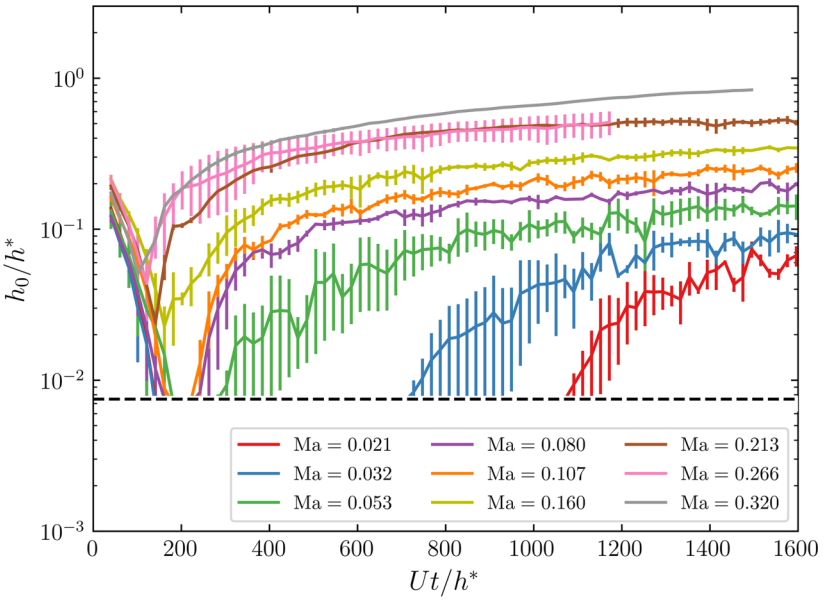

FIG. 6. Plot of the experimental centerline film thickness $\bar{h}_0 = h(0,t)/h^*$ against time $\bar{t}$ for a 1.00 cSt/5.00 cSt mixture ($\mathrm{Ev} = 2.6 \times 10^{-3}$) at several values of the Marangoni number $\mathrm{Ma} = 0.021$–0.320 ($\phi_\infty = 0.02\%$–0.30%). The other dimensionless parameters for a 1.00 cSt/5.00 cSt mixture are reported in Table II. Experimental data cannot be obtained for thicknesses below the dotted line at $\bar{h} \simeq 7.5 \times 10^{-3}$ ($h \simeq 90$ nm). Error bars represent the standard deviation obtained from multiple data sets.

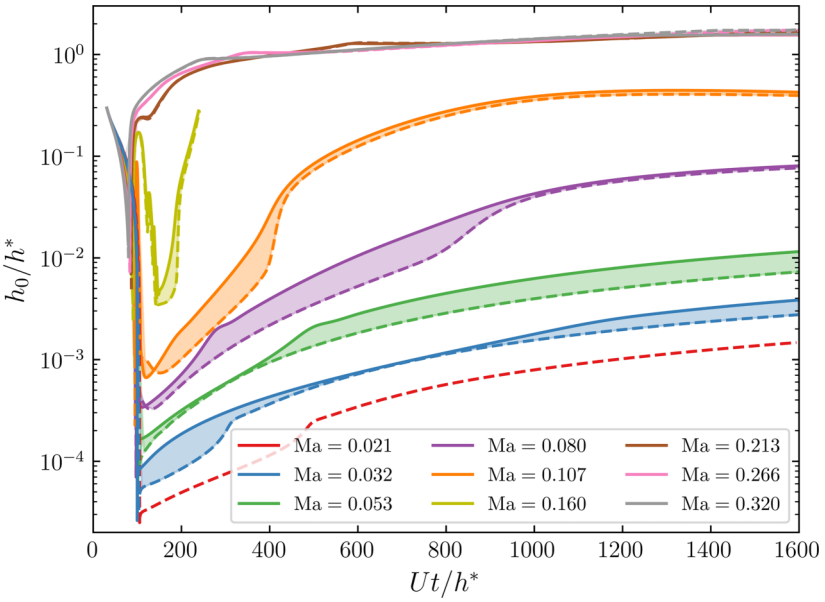

FIG. 7. Plot of the theoretical centerline film thickness $\bar{h}_0 = h(0,t)/h^*$ against time $\bar{t}$ for several values of the Marangoni number $\mathrm{Ma} = 0.021$–0.320 ($\phi_\infty = 0.02\%$–0.30%). The solid lines correspond to $\mathrm{Ha} = 1.6 \times 10^{-5}$, the dashed lines correspond to $\mathrm{Ha} = 1.6 \times 10^{-6}$, and the region in between two curves of the same color is shaded to guide the eye. The other dimensionless parameters are $\mathrm{Ca} = 2.4 \times 10^{-6}$, $\mathrm{Pe} = 10^3$, $\mathrm{Bo} = 4.3 \times 10^{-2}$, and $\mathrm{Ev} = 2.6 \times 10^{-3}$, corresponding to a 1.00 cSt/5.00 cSt mixture (reported in Table II).

However, the larger growth rates measured in the experiments suggest a stronger driving force for film flow, potentially due to a stronger Marangoni flux than that which is predicted theoretically.

It is expected that several assumptions of the model break down at low Ma due to the fact that ϕ is not small locally. For example, the mixture properties cannot be accurately approximated by the solvent properties (ρ, μ, and γ_0). Between the pure solvent ($\phi = 0$) and pure solute ($\phi = 1$), the fluid density can increase by at most 20%, while the viscosity can undergo a tenfold increase. Moreover, the simple linear relationship (4) relating γ and ϕ breaks down when ϕ is not small. The slope of the $O(\phi)$ term, which is estimated to be the difference in surface tensions $\gamma_1 - \gamma_0$, may also be inaccurate. These errors are compounded by the uncertainties in D and A, which may introduce quantitative (though not qualitative) changes to the rate of film growth.

C. Mound volume and flux

The centerline film thickness h_0 gives a measure of film growth, but cannot quantify the volumetric flux of material into the solute-enriched apical mound. For the axisymmetric profiles considered here, we quantify the volumetric flux by defining the mound volume

$$V(t) = 2\pi \int_0^R h(r,t) r \, dr, \tag{15}$$

where R is the mound radius, defined by $h(R,t) = h_{\min}$, the minimum film thickness. We define the time at which the mound forms (i.e., when V begins to increase as a function of time) by $t = t_M$, whence $V(t_M) = V_M$. The volumetric flow rate into the mound is given by dV/dt. By mass conservation,

$$\frac{dV}{dt} = \frac{d(V - V_M)}{d(t - t_M)} \approx -\pi R^2 E(1 - \phi_M) + 2\pi R q, \tag{16}$$

where ϕ_M is the solute concentration in the mound and

$$q = \left(\frac{h^3}{3\mu} \frac{\partial p}{\partial r} - \frac{h^2}{2\mu} \frac{\partial \gamma}{\partial r} \right) \Bigg|_{r=R} \tag{17}$$

is the net volumetric flux per unit circumference. Equation (16) can be obtained by multiplying (2) by $2\pi r dr$, integrating from $r = 0$ to R (assuming R is a weak function of t), and approximating $\phi \approx \phi_M = \text{const}$ in $0 \leqslant r \leqslant R$ (i.e., neglecting the dependence of ϕ on r inside the mound volume). Thus, the rate of change of V gives an aggregate measure of the net evaporation of solvent through the projected area πR^2 and the net influx of fluid (due to pressure and surface-tension gradients) through the perimeter $2\pi R$. Rendering r, t, and h dimensionless according to (8) yields the dimensionless variables $\overline{V} = V/[\pi a (h^*)^2]$, $\overline{V}_M = V_M/[\pi a (h^*)^2]$, and $\bar{t}_M = t_M U/h^*$.

Figure 8 shows experimental measurements and simulation data of the dimensionless excess mound volume flux $d\overline{V}/d\bar{t}$ plotted against Ma at three different values of Ev, corresponding to the three silicone oil blends presented in Table II. For all values of Ev, the flow rate increases with increasing Ma, in agreement with our previous results. The data fall within the intermediate and capillary regimes, as discussed previously. (Since little to no mound formation is observed in the van der Waals regime, a mound volume flux cannot be computed.) In all of the reported experimental measurements, the mound volume grows linearly with time throughout the duration of each experiment and thus the flux $d\overline{V}/d\bar{t}$ is approximately constant with time. By contrast, in the theoretical calculations the dimensionless volume varies nonlinearly with time. The simulation values reported in Fig. 8 correspond to the flux at $\bar{t} = \bar{t}_M$, the inception point of mound formation. For the simulation data, two values of Ha are shown for comparison, since the Hamaker constant A is uncertain in the experimental measurements.

The intermediate regime is where the film thins to a nanoscopic thickness, followed by significant film regeneration and mound volume growth. In accord with the experimental results outlined in Sec. IV A, the range of Ma in the intermediate regime decreases with decreasing evaporation rate.

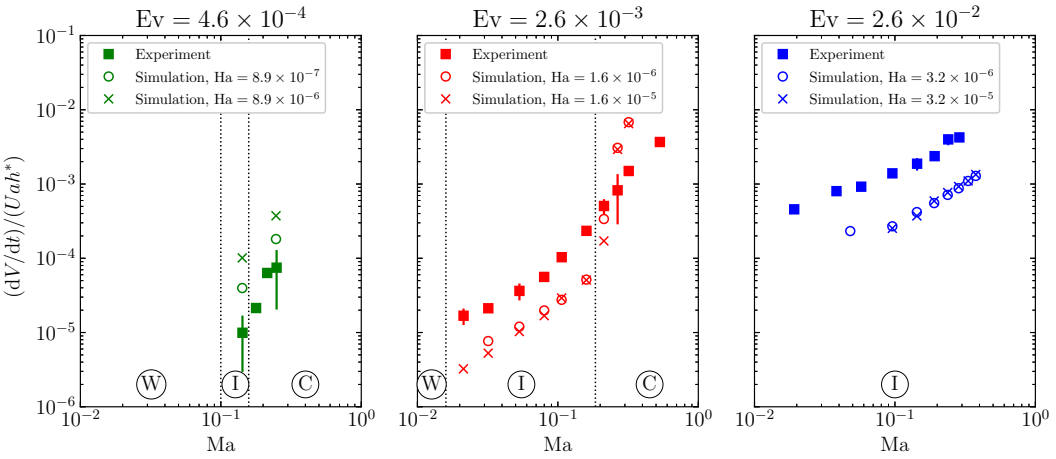

FIG. 8. Experimental and simulation data of the dimensionless mound volume flux $d\overline{V}/d\bar{t} = (1/ah^*U)(dV/dt)$ against Ma for 1.50 cSt/10.0 cSt (Ev $= 4.6 \times 10^{-4}$), 1.00 cSt/5.00 cSt (Ev $= 2.6 \times 10^{-3}$), and 0.65 cSt/5.00 cSt (Ev $= 2.6 \times 10^{-2}$) mixtures. Other relevant dimensionless parameters appear in Table II. The symbols Ⓦ, ①, and Ⓒ stand for the van der Waals, the intermediate, and the capillary regimes, respectively. The closed squares correspond to experimental measurements and the error bars represent the standard deviation obtained from multiple data sets. In all of the experimental measurements reported, the dimensionless mound volume $\overline{V}$ increases linearly with time. For each value of Ev in the simulations, two values of Ha are shown for comparison. Simulation data are shown by circles for low Ha and by crosses for high Ha. In the numerical computations, $\overline{V}$ typically increases nonlinearly with time; thus, the symbols represent the finite-difference approximant of $d\overline{V}/d\bar{t}$ at $\bar{t} = \bar{t}_M$, the inception point of mound formation.

For all three evaporation rates, the simulations underpredict the mound volume flux when compared to the experiments. We attribute the quantitative differences between theory and experiment to errors associated with the simplifying assumptions made in the model (see Sec. IV B). For a given value of Ma, the mound volume flux increases with the evaporation rate. From examining the first term on the right-hand side of (16), it would appear that increasing Ev would result in a decreasing flow rate. However, increasing Ev also *increases* the flow rate through coupling between evaporation and the pressure- and surface-tension-driven fluxes. In other words, the *direct* contribution of solvent evaporation to the rate of change of the mound volume is small relative to the *indirect* contribution through coupling with the flux. Similar trends are seen in [4], where higher rates of evaporation cause surface-tension gradients to develop at earlier times, leading to a faster film growth.

As Ma increases, we move into the capillary regime, where the dominant contribution to the pressure comes from capillarity. In this regime, the theory suggests a stronger dependence of $d\overline{V}/d\bar{t}$ on Ma than what is observed in the experiments [Figs. 8(b) and 8(c)]. These discrepancies are likely not associated with uncertainties in the Hamaker constant, since at high Ma the fluxes become insensitive to Ha. However, since the evolution of the film thickness and solute concentration is highly nonlinear and fully coupled, it is not clear at present which of these simplifications are most significant.

V. DISCUSSION

Evaporation of a pure silicone oil over a glass substrate uniformly depletes the liquid down to a nanoscopically thin film that is stabilized by a disjoining pressure. For a binary mixture of silicone oils, evaporation of the volatile component preferentially concentrates the nonvolatile solute in regions where the liquid film is thinnest. Thus, the thin-film region experiences larger changes in composition as compared to the bulk. Gradients in solute concentration in turn create gradients in surface

tension that drive Marangoni flows. In the mixtures studied presently, the solute-rich areas have larger surface tensions because the nonvolatile solute has a higher surface tension than the solvent.

Qualitative agreement between the experiments and the theoretical predictions was obtained. Namely, the dependence of the film dynamics on the solutocapillary Marangoni number Ma and the dimensionless evaporative velocity Ev is reproduced in our model. The theoretical results show clearly that the transitions between the different flow regimes are distinguished by dominant contributions to the dynamic pressure and the interplay between pressure- and surface-tension-driven flows. These different regimes are tuned by the Marangoni number. We found that increasing Ma increases the flux at the mound radius and hence the rate of film growth, in accord with previous studies [19]. The theory and the experiments also indicate that within each regime, increasing Ev increases the rate of film growth and the Marangoni flux through nonlinear coupling. This effect is augmented at higher Ev because the timescale of solvent depletion during evaporation becomes small when compared to the diffusive timescale ($\mathrm{Pe}^{-1} \ll \mathrm{Ev}$). Since diffusion is incapable of attenuating gradients in species concentration generated by the evaporating fluid, smaller values of Ma are sufficient to generate a Marangoni flow that accumulates fluid in an apical mound. The rate of film growth was quantified in Figs. 6 and 7 (in terms of the centerline height) and in Fig. 8 (in terms of the mound volume flux).

Quantitative differences between the theory and experiments are observed. Specifically, in the intermediate and the capillary regimes, the model respectively under- and overestimates the excess mound volume flux for a fixed evaporation rate (Fig. 8). Several explanations were given as to the failure of the model to quantitatively reproduce what is seen in the experiments. First, we assumed that the mixture properties could be replaced with properties of the solvent. This simplification is expected to hold when ϕ is small. However, as is shown in Fig. 5, ϕ can approach unity locally when Ma is small. Weak Marangoni and diffusive fluxes prevent the mixture from rehomogenizing. Significantly, the viscosities of the two components are not similar; it is expected that solute accumulation viscosifies the mixture locally.

Second, both the evaporation model and the surface-tension model used in the present study are simplistic. The former is an approximation of the full mass-transfer problem involving species transport in both the liquid and vapor phases. The latter was obtained from a linear interpolation between the two pure-component surface tensions γ_1 and γ_0. The rate of change of γ per unit increment in ϕ is not necessarily equal to the difference $\gamma_1 - \gamma_0$, as is assumed here. A more accurate model would require measurements of the surface-tension isotherms as a function of mixture concentration. Attempts to experimentally obtain this isotherm were made on our part, in which a pendant bubble of air was suspended in a binary silicone oil solution and the surface tension was measured as a function of composition. However, since the relative change in surface tension with composition is quite small, an empirical mixing rule beyond the linear formulation in Eq. (4) was not revealed.

Uncertainty in the estimated values for the binary diffusivity D and the Hamaker constant A could also lead to a departure between experiments and the theory. Errors in the binary diffusivity are expected to matter most when the timescale of species diffusion becomes comparable to the timescale in which evaporation induces gradients in species concentration. In other words, uncertainties in D will play a larger role whenever the film thickening-thinning dynamics are slow. This effect is more pronounced either at low rates of evaporation or at sufficiently low Ma, when Marangoni effects are weak. Errors in the Hamaker constant A have a greater effect in the thinner areas of the film where disjoining pressure dominates. To address this issue, we conducted simulations at two different values of the dimensionless Hamaker constant Ha, covering the estimated range of A for the silicone oil systems.

Finally, the expression for the disjoining pressure used in Eq. (5) is only valid for films with thicknesses $\gtrsim$1 nm. Near this limit, short-range interactions may come into play that are not taken into account in our model. For example, for the parameters in this study, the rate of evaporation is expected to dramatically decrease when the film thickness $\lesssim$ 1 nm [34]. These effects are expected to matter in the van der Waals regime and at low Ma prior to mound formation in the intermediate regime.

VI. CONCLUSION

Experiments with binary, low-molecular-weight silicone oil mixtures have revealed the presence of solutocapillary flows in ultrathin films. Evaporative loss of the volatile solvent leads to concentration inhomogeneities that give rise to spatial surface-tension gradients. Under these conditions, we were able to examine the interplay between the rate of evaporation and the bulk solute fraction of the nonvolatile oil and identify three distinct regimes of behavior. However, experimental measurements were not able to convey information regarding local surface species concentration and the relative importance of different physical forces. Thus, we took advantage of the lubrication approximation to develop a thin-film theory that can simultaneously describe fluid flow and species concentration.

Our experimental and numerical results highlight several general trends. Under all conditions examined, the film thickness *increases* for some period of time at the centerline, against the action of gravitational and capillary forces. There are two driving forces which can account for the flow reversal: (i) disjoining pressure due to the van der Waals interaction between the substrate and the upper free surface when the film becomes nanoscopically thin and (ii) Marangoni stresses due to a solute concentration gradient at the upper free surface. If the dimensionless evaporative velocity Ev is a control parameter (i.e., the solvent volatility is fixed), then the extent to which these two forces contribute to flow reversal depends on the magnitude of the Marangoni number Ma (experimentally, Ma is controlled by the amount of solute initially added to the mixture).

The present work can be extended in several ways. First, improvements to the model (addressing some or all of the shortcomings mentioned in the discussion) could lead to a more quantitative comparison. However, we do not expect such changes to modify the essential physics described by our model. Second, the dependence of the flow physics on the other dimensionless groups, e.g., Ca, Bo, Pe, and Ha, could be explored. Additionally, the effect of evaporation in surfactant-laden flows could be investigated. In systems with soluble surfactants, mass loss due to evaporation could potentially induce surfactant transport towards the interface, ultimately affecting the surface distribution of surfactant and the resulting interfacial Marangoni stresses. Finally, it would be interesting to examine how the results of the present work, which considers the interaction between solid-liquid and air-liquid interfaces, apply to a system with two air-liquid interfaces, such as the foam flows considered in Ref. [37]. In such systems, van der Waals forces result in a conjoining pressure (a destabilizing effect), which would presumably compete with Marangoni stresses. The reduced traction due to the presence of two mobile surfaces is expected to qualitatively change the fluid dynamics.

ACKNOWLEDGMENTS

This work was funded by the National Science Foundation under Grant No. CBET-1435683. Part of this work was performed at the Stanford Nano Shared Facilities, supported by the National Science Foundation under Award No. ECCS-1542152. J.M.B. was supported by a Graduate Research Fellowship from the National Science Foundation. M.R.-H. and X.S. were partially supported by Beijing Welltrailing Science and Technology Company. M.R.-H. and G.G.F. thank Dr. David Vazquez, Prof. Amy Shen, and Professor Eliot Fried for hosting M.R.-H. at the Okinawa Institute of Science and Technology Graduate University and for their assistance in performing experiments with the FLIR T650sc thermal camera. M.R.-H. and G.G.F. would also like to express their appreciation and gratitude to Prof. Stergios G. Yiantsios at the Aristotle University of Thessaloniki (AUTh) for his support and collaboration in developing the theoretical model and for his hospitality and mentorship throughout M.R.H.'s visit to AUTh.

[1] J. Thomson, On certain curious motions observable at the surfaces of wine and other alcoholic liquors, Philos. Mag. **10**, 330 (1855).

[2] J. B. Fournier and A. M. Cazabat, Tears of wine, Europhys. Lett **20**, 517 (1992).
[3] P. G. de Gennes, Instabilities during the evaporation of a film: Non-glassy polymer + volatile solvent, Eur. Phys. J. E **6**, 421 (2001).
[4] M. H. Eres, D. E. Weidner, and L. W. Schwartz, Three-dimensional direct numerical simulation of surface-tension-gradient effects on the leveling of an evaporating multicomponent fluid, Langmuir **15**, 1859 (1999).
[5] W. S. Overdiep, The levelling of paints, Prog. Org. Coat. **14**, 159 (1986).
[6] S. D. Howison, J. A. Moriarty, J. R. Ockendon, E. L. Terrill, and S. K. Wilson, A mathematical model for drying paint layers, J. Eng. Math. **32**, 377 (1997).
[7] P. L. Evans, L. W. Schwartz, and R. V. Roy, A mathematical model for crater defect formation in a drying paint layer, J. Colloid Interface Sci. **227**, 191 (2000).
[8] A. Oron, S. H. Davis, and S. G. Bankoff, Long-scale evolution of thin liquid films, Rev. Mod. Phys. **69**, 931 (1997).
[9] R. V. Craster and O. K. Matar, Dynamics and stability of thin liquid films, Rev. Mod. Phys. **81**, 1131 (2009).
[10] H. Hu and R. G. Larson, Evaporation of a sessile droplet on a substrate, J. Phys. Chem. B **106**, 1334 (2002).
[11] H. Hu and R. G. Larson, Analysis of the effects of Marangoni stresses on the microflow in an evaporating sessile droplet, Langmuir **21**, 3972 (2005).
[12] H. Hu and R. G. Larson, Marangoni effect reverses coffee-ring depositions, J. Phys. Chem. B **110**, 7090 (2002).
[13] M. Majumder, C. S. Rendall, J. A. Eukel, J. Y. L. Wang, N. Behabtu, C. L. Pint, T. Y. Liu, A. W. Orbaek, F. Mirri, J. Nam, A. R. Barron, R. H. Hauge, H. K. Schmidt, and M. Pasquali, Overcoming the "coffee-stain" effect by compositional Marangoni-flow-assisted drop-drying, J. Phys. Chem. B **116**, 6536 (2012).
[14] R. G. Larson, Transport and deposition patterns in drying sessile droplets, AIChE J. **60**, 1538 (2014).
[15] S. K. Serpetsi and S. G. Yiantsios, Stability characteristics of solutocapillary Marangoni motion in evaporating thin films, Phys. Fluids **24**, 122104 (2012).
[16] L. G. Leal, *Advanced Transport Phenomena: Fluid Mechanics and Convective Transport Processes* (Cambridge University Press, Cambridge, 2007).
[17] C. J. Parks and P. C. Wayner, Jr., Surface shear near the contact line of a binary evaporating curved thin film, AIChE J. **33**, 1 (1987).
[18] R. Vuilleumier, V. Ego, L. Neltner, and A. M. Cazabat, Tears of wine: The stationary state, Langmuir **11**, 4117 (1995).
[19] X. Fanton and A. M. Cazabat, Spreading and instabilities induced by a solutal Marangoni effect, Langmuir **14**, 2554 (1998).
[20] A. E. Hosoi and J. W. M. Bush, Evaporative instabilities in climbing films, J. Fluid Mech. **442**, 217 (2001).
[21] J. J. Nichols and P. E. King-Smith, Thickness of the pre- and post-contact lens tear film measured in vivo by interferometry, Invest. Ophth. Vis. Sci. **44**, 68 (2003).
[22] E. Hermans, M. S. Bhamla, P. Kao, G. G. Fuller, and J. Vermant, Lung surfactants and different contributions to thin film stability, Soft Matter **11**, 8048 (2015).
[23] M. S. Bhamla, C. Chai, N. I. Rabiah, J. M. Frostad, and G. G. Fuller, Instability and breakup of model tear films, Invest. Ophth. Vis. Sci. **57**, 949 (2016).
[24] R. J. Fullard and C. Snyder, Protein levels in nonstimulated and stimulated tears of normal human subjects, Invest. Ophth. Vis. Sci. **31**, 1119 (1990).
[25] A. Oron and S. G. Bankoff, Dewetting of a heated surface by an evaporating liquid film under conjoining/disjoining pressures, J. Colloid Interface Sci. **218**, 152 (1999).
[26] P. G. de Gennes, Wetting: Statics and dynamics, Rev. Mod. Phys, **57**, 827 (1985).
[27] S. Y. Heriot and R. A. L. Jones, An interfacial instability in a transient wetting layer leads to lateral phase separation in thin spin-cast polymer-blend films, Nat. Mater. **4**, 782 (2005).
[28] U. Thiele, Thin film evolution equations from (evaporating) dewetting liquid layers to epitaxial growth, J. Phys.: Condens. Matter **22**, 084019 (2010).
[29] L. M. Pismen, Spinodal dewetting in a volatile liquid film, Phys. Rev. E **70**, 021601 (2004).

[30] N. Samid-Merzel, S. G. Lipson, and D. S. Tannhauser, Pattern formation in drying water films, Phys. Rev. E **57**, 2906 (1998).
[31] A. M. Cazabat, N. Fraysse, F. Heslot, P. Levinson, J. Marsh, F. Tiberg, and M. P. Valignat, Pancakes, Adv. Colloid Interface Sci. **48**, 1 (1994).
[32] A. Sharma and A. T. Jameel, Nonlinear stability, rupture, and morphological phase separation of thin fluid films on apolar and polar substrates, J. Colloid Interface Sci. **161**, 190 (1993).
[33] M. Elbaum and S. G. Lipson, How Does a Thin Wetted Film Dry Up? Phys. Rev. Lett. **72**, 3562 (1994).
[34] A. Sharma, Equilibrium and dynamics of evaporating and condensing thin fluid domains: Thin film stability and heterogeneous nucleation, Langmuir **14**, 4915 (1998).
[35] J. Lopez, C. A. Miller, and E. Ruckenstein, Spreading kinetics of liquid drops on solids, J. Colloid Interface Sci. **56**, 460 (1976).
[36] T. T. Chau, W. J. Bruckard, P. T. L. Koh, and A. V. Nguyen, A review of factors that affect contact angle and implications for flotation practice, Adv. Colloid Interface Sci. **150**, 106 (2009).
[37] J. M. Frostad, D. Tammaro, L. Santollani, S. Bochner de Araujo, and G. G. Fuller, Dynamic fluid-film interferometry as a predictor of bulk foam properties, Soft Matter **12**, 9266 (2016).
[38] See Supplemental Material at http://link.aps.org/supplemental/10.1103/PhysRevFluids.4.034002 for additional details on the experimental protocol, ellipsometry measurements, thermocapillary and evaporation data for pure silicone fluids, representative experimental videos, examples of symmetry-breaking flow instabilities, derivation of the governing equations, small-deformation analysis, and details on the numerical method (logarithmic formulation, coordinate transformation, and numerical integration).
[39] E. Ricci, R. Sangiorgi, and A. Passerone, Density and surface tension of dioctylphthalate, silicone oil, and their solutions, Surf. Coat. Technol. **28**, 215 (1986).
[40] A. M. Cazabat, How does a droplet spread? Contemp. Phys. **28**, 347 (1987).
[41] C. Berdan II and L. G. Leal, Motion of a sphere in the presence of a deformable interface, J. Colloid Interface Sci. **87**, 62 (1982).
[42] N. Rashidnia, R. Balasubramaniam, J. Kuang, P. Petitjeans, and T. Maxworthy, Measurement of the diffusion coefficient of miscible fluids using both interferometry and Wiener's method, Int. J. Thermophys. **22**, 547 (2001).
[43] F. Ilinca and D. Pelletier, Positivity preservation and adaptive solution of two-equation models of turbulence, Int. J. Therm. Sci. **38**, 560 (1999).
[44] R. Fattal and R. Kupferman, Constitutive laws for the matrix-logarithm of the conformation tensor, J. Non-Newtonian Fluid Mech. **123**, 281 (2004).
[45] M. A. Hulsen, R. Fattal, and R. Kupferman, Flow of viscoelastic fluids past a cylinder at high Weissenberg number: Stabilized simulations using matrix logarithms, J. Non-Newtonian Fluid Mech. **127**, 27 (2005).
[46] R. G. Cox and H. Brenner, The slow motion of a sphere through a viscous fluid towards a plane surface II. Small gap widths, including inertial effects, Chem. Eng. Sci. **22**, 1753 (1967).
[47] D. E. Kataoka and S. M. Troian, A theoretical study of instabilities at the advancing front of thermally coated films, J. Colloid Interface Sci. **192**, 350 (1997).
[48] A. Hamraoui, M. Cachile, C. Poulard, and A. M. Cazabat, Fingering phenomena during spreading of surfactant solutions, Colloid. Surf. A **250**, 215 (2004).
[49] A. M. Cazabat, F. Heslot, P. Carles, and S. M. Troian, Hydrodynamic fingering instability of driven wetting films, Adv. Colloid Interface Sci. **39**, 61 (1992).
[50] M. Cachile, M. Schneemilch, A. Hamraoui, and A. M. Cazabat, Films driven by surface tension gradients, Adv. Colloid Interface Sci. **96**, 59 (2002).
[51] M. R. E. Warner, R. V. Craster, and O. K. Matar, Fingering phenomena associated with insoluble surfactant spreading on thin liquid films, J. Fluid Mech. **510**, 169 (2004).
[52] J. L. Joye, G. J. Hirasaki, and C. A. Miller, Dimple formation and behavior during axisymmetrical foam film drainage, Langmuir **8**, 3083 (1992).